PSF monitoring and in-focus wavefront control for NGST

Catherine M. Ohara*, David C. Redding, Joseph J. Green, and Fang Shi
Jet Propulsion Laboratory; 4800 Oak Grove Dr., Pasadena, CA 91109

ABSTRACT

A technique for measuring the low-order wavefront aberrations in segmented-mirror telescopes using in-focus point-spread functions – "PSF Monitoring" – has been developed for the Next Generation Space Telescope (NGST). PSF Monitoring will utilize the star images in science data to monitor the evolving wavefront error and determine when a full wavefront sensing and control update is necessary. It also has the potential for in-focus wavefront control – that is, the science images may themselves provide inputs to the wavefront control process. This paper presents the results of our experiments and simulations on the NGST Wavefront Control Testbed (WCT) to demonstrate PSF Monitoring and in-focus wavefront control. In particular, we describe the capture range and accuracy observed on WCT, as well as a two-wavelength algorithm that has been used to extend the piston capture range. A real-time PSF Monitoring and control experiment on WCT is also presented.

Keywords: NGST, wavefront sensing, space telescope, segmented mirror, point spread function

1. INTRODUCTION

The Next Generation Space Telescope (NGST) will utilize a large, deployed, 6-meter aperture with actively controlled mirror segments to provide significant advances in our knowledge of the universe. These mirror segments will be aligned, phased, and fine-figured to the diffraction limit at 2-μm using the wavefront sensing and control (WFS&C) methods described in Ref. 1.

Because of its passive thermal control system and benign orbit at L2, the telescope's mirror alignment is expected to remain adequately stable for long-duration science observations. However, small drifts and alignment errors will gradually accumulate; thus, periodic WFS&C observations will need to be performed. "PSF Monitoring" can identify when to perform WFS&C, by using the point-spread functions (PSFs) available in science data to measure the evolving RMS wavefront error. An extension of PSF Monitoring – in-focus wavefront control – will use the PSFs to explicitly determine the low-order wavefront aberrations. This would allow the science images to be part of the WFS&C process, thereby reducing the amount of engineering observing time needed to realign the primary mirror.

This paper reports the results of PSF Monitoring and in-focus wavefront control experiments on the NGST Wavefront Control Testbed[2] (WCT). These results show very good performance in controlling the lowest-order wavefront errors, namely piston, tip, and tilt of each of the three WCT segments. The laboratory results are well predicted by our computer models of the system – indeed, models are used to determine the control using prescription retrieval techniques, as discussed in Section 2. Section 3.1 provides a brief overview of the WCT hardware. Sections 3.2 to 3.4 describe our experiments and simulations to characterize the wavefront sensing capture range and accuracy. A two-wavelength algorithm to extend the piston capture range is discussed in Section 3.5. A real-time PSF monitoring and control experiment is presented in Section 3.6. Closing remarks are presented in Section 4.

2. METHODOLOGY

To perform PSF Monitoring on WCT, we use a technique called "prescription retrieval," realized in an "In-focus PSF Optimizer" (IPO) algorithm. Prescription retrieval is a process whereby an optical prescription-based computer model of a system is driven to match a set of image data by direct optimization of model parameters. The retrieved prescription

* Catherine.M.Ohara@jpl.nasa.gov

can then be used to compute the wavefront and to compute the control needed to correct the wavefront errors. It is an indirect parametric phase retrieval process, in which the phase is inferred from the converged prescription.

Prescription retrieval was originally developed to analyze Hubble Space Telescope (HST) images following discovery of its aberrated primary mirror[3]. It was successful in measuring key HST parameters, especially the spherical aberration of the primary mirror and the repeater camera optics. By estimating and removing the contribution of the repeater optics to the total spherical aberration, prescription retrieval was successful in determining the conic constant of the primary mirror.

Prescription retrieval seeks to minimize a cost function that penalizes the mismatch between a model-generated image and an actual data image. The model images can be generated by an optical analysis code such as MACOS[4], which uses ray-trace and Fourier analysis to produce accurate images from optical prescription data.

An alternative approach for systems that do not experience large motions is to use linear sensitivity-matrices to generate the model images. This is the approach preferred for IPO, as linear models are faster to compute. Linear models are limited by the small-angle approximation to parameter excursions that cause ray angle deviations much less than 1 degree. This limit permits good model accuracy over several waves of aberration, far greater than IPO, which is designed to operate near the diffraction limit, will normally experience.

The linear model used for IPO generates the exit-pupil wavefront in vector form, as the product of a sensitivity matrix $d\boldsymbol{w}/d\boldsymbol{x}$ and an optical state vector $\boldsymbol{x}$, plus the nominal wavefront vector $\boldsymbol{w}_0$:

$$\boldsymbol{w} = \frac{d\boldsymbol{w}}{d\boldsymbol{x}}\,\boldsymbol{x} + \boldsymbol{w}_0 \tag{1}$$

The $\boldsymbol{w}$ vector consists of the non-zero elements of the wavefront matrix, reordered into columns. Each column of the sensitivity matrix $d\boldsymbol{w}/d\boldsymbol{x}$ represents the influence on the overall wavefront of the corresponding element of the state vector $\boldsymbol{x}$. The state vector contains the prescription parameters of interest (such as segment tip, tilt, and piston,) segment figure parameters, and alignment and figure parameters for other optics. The sensitivity matrix can be computed directly from the optical prescription, generated by numerical differentiation using MACOS, or directly measured using wavefront sensing on the actual hardware. Similarly, $\boldsymbol{w}_0$ can be computed from the optical prescription or measured using wavefront sensing. In the latter case, it may be the result of the previous application of prescription retrieval, so that $\boldsymbol{w}$ represents the deviation from the previous measurement.

The wavefront $\boldsymbol{w}$ is converted to phase and then combined with a pupil image (either measured or simulated) to create a complex pupil field. The pupil field is propagated to the image plane using a Fast-Fourier Transform-based far-field (Fresnel) transform. The image is computed from the modulus squared of the image-plane complex field, blurred by jitter and other effects, and resampled to the detector pixel scale. Sampling of the pupil and zero padding of the complex amplitude matrix are chosen so that the binning step does not cross pixel boundaries.

The choice of degrees-of-freedom, corresponding to elements in the state vector $\boldsymbol{x}$, has a significant impact on the accuracy and utility of prescription retrieval in general. For IPO on WCT-2, the linear model degrees of freedom are piston, tip, and tilt for each of the three segments. These low spatial frequency parameters receive significant signal in the in-focus images and produce unambiguous signatures in the data.

IPO pre-processing eliminates some other degrees of freedom. Background radiation in the image is identified and removed from the data. Image intensity is also removed in IPO, by normalizing the data and model PSFs at every step. Global tip-tilt is removed by centering the images in the data frame. The next sections of this report describe the performance of IPO on the WCT-2 hardware.

3. RESULTS FROM WCT-2

3.1 Overview of WCT-2

WCT provides a segmented optics platform for the development, testing, and validation of our in-focus WFS&C algorithms. A detailed hardware description can be found in Ref. 2. Here, we briefly review the key components of the segmented mirror system, WCT-2.

The WCT-2 "primary mirror" consists of 3 sparsely separated mirror segments (Figure 1). Each segment is controlled in the rigid-body degrees of freedom by 3 piezoelectric translators (PZTs). The PZTs have a repeatability of 5-nm and a full travel range of 12,000 nm[5]. The excellent accuracy of the PZTs has been exploited in several experiments, described in Sections 3.4 and 3.5.

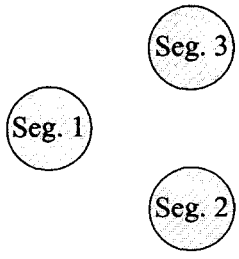

Figure 1: WCT-2 mirror numbering scheme used by IPO.

The testbed uses a Xenon light source, imaged through a 5-μm diameter pinhole. The blur effects of this slightly resolved source are incorporated into the IPO model by using a convolution model with a Gaussian half-width of 0.54 pixels.

Several experiments utilized the testbed's "PSF magnifier" – two additional lenses which can be inserted into the optical path to magnify the PSF by 4.5 times. This provides an extremely well sampled PSF with which to refine our in-focus WFS&C algorithms.

Lab seeing and jitter effects are partially removed by co-adding several short-exposure frames. This is an essential pre-processing step for non-magnified data, since the PSF is under-sampled and spans only a few pixels. An exposure time of 0.1 seconds is used when taking non-magnified data; 3 seconds when the PSF magnifier is in place.

3.2 Piston Capture Range

"Capture range" refers to the maximum phase error that can be reliably sensed and controlled. In terms of segment piston, the capture range is the largest piston height that can be detected without any phase ambiguity. If the piston height between two adjacent segments is within the capture range, then IPO can successfully align the segment. If the piston height exceeds the capture range, then the measured piston values will be incorrect, or "wrap," by a factor of $\lambda/2$ (surface, not wavefront).

The piston capture range on WCT-2 is demonstrated qualitatively in the following simulation. In-focus images were generated from the WCT-2 computer model at several Seg. #2 piston positions (Figure 2). Photon noise and 30 electrons of CCD read noise were included. The images were then analyzed with IPO. Figure 3 shows the simulation results: the detected piston for Seg. #2 is plotted against the actual piston value. The "sawtooth" pattern arises from the half-wave ambiguity – when the step height is larger than $\pm\lambda/4$, the IPO-detected piston values become "wrapped" by $\lambda/2$. This simulation example also suggests that IPO may return an incorrect result if the segment piston is exactly at the end of its capture range.

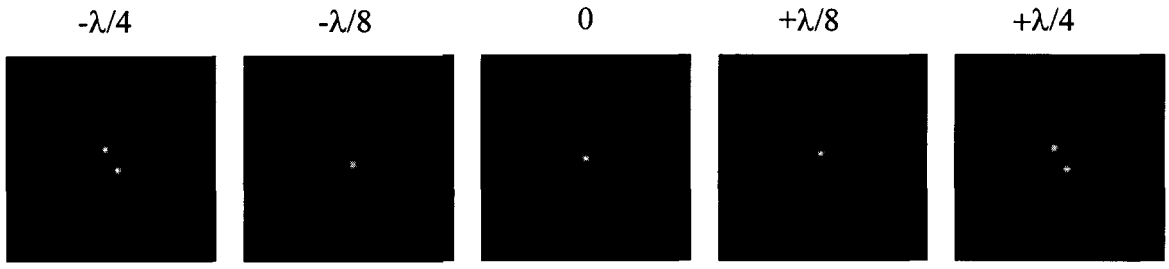

Figure 2: Simulated WCT-2 images (monochromatic, with PSF magnifier) showing a range of Seg. #2 piston errors.

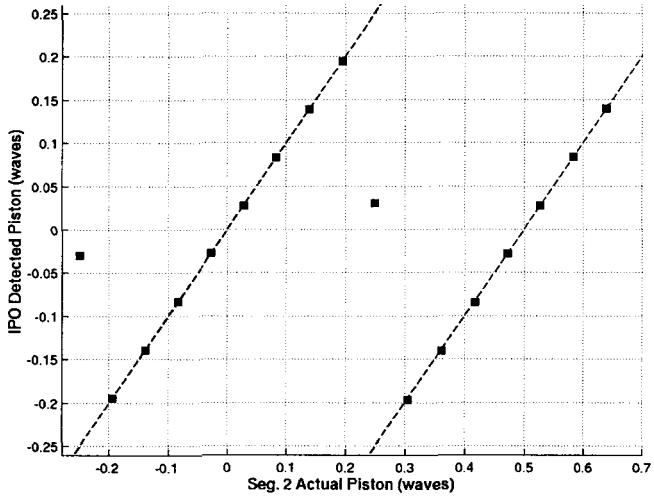

Figure 3: Piston capture range simulation (monochromatic).

Experiments on WCT-2 have confirmed that the piston capture range is ±λ/4 when using narrowband data. The longest wavelength filter on the testbed, 900±20 nm, provides a large capture range of ±225 nm – well within the accuracy of the Dispersed Fringe Sensor coarse phasing algorithm[6]. Two-wavelength IPO can be used to extend the piston capture range even further; this will be discussed in Section 3.5.

3.3 Tip/Tilt Capture Range

Whereas the piston capture range (for narrowband measurements) is mostly influenced by the wavelength, the tip/tilt capture range can depend critically on several factors, including the pixel sampling, the plate scale, and the signal-to-noise ratio. On WCT-2, the tip/tilt capture range varies from 4 arcseconds without the PSF magnifier to 5 arcseconds with the PSF magnifier.

The simulation below illustrates the difference between magnified and non-magnified IPO performance. Images were generated from the model using a range of Seg. #2 x-tilt positions. Two in-focus images – magnified and non-magnified – were generated for each x-tilt position. Figure 4 shows the detected x-tilt versus the expected value. Without the PSF magnifier, IPO was able to detect the correct x-tilt up to 4 arcseconds. With the magnifier, however, IPO successfully detected the x-tilt out to 5 arcseconds. These simulations are consistent with the tip/tilt capture range observed on the WCT hardware.

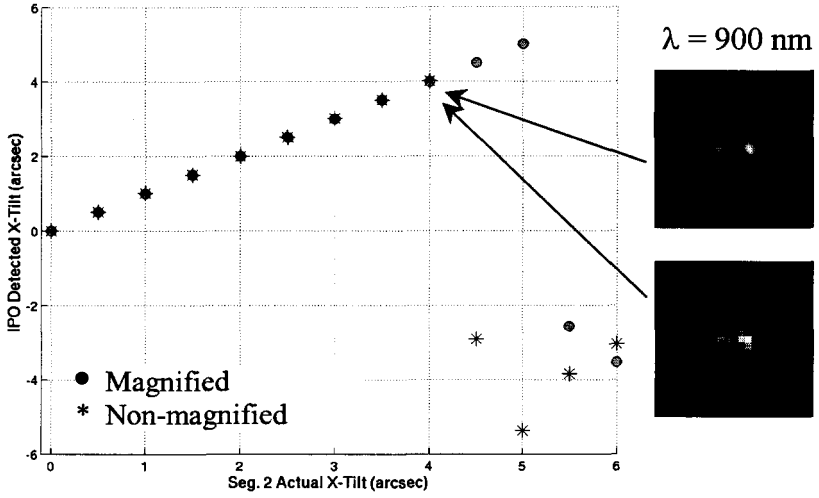

Figure 4: Tip/tilt capture range simulation, with/without PSF Magnifier (monochromatic).

3.4 Wavefront Sensing Accuracy

Experiments and simulations have been conducted to study IPO's wavefront sensing accuracy on WCT-2. In the experiments, one of the three mirror segments was pistoned or tilted by a known amount, by sending commands to the 3 PZTs controlling that segment. IPO data was taken both before and after moving the test segment. The difference in IPO's piston/tip/tilt estimates between the "before" and "after" data images was then compared to the applied segment movement. In each experiment, the piston or tip/tilt command was chosen to be larger than the 5 nm accuracy of the PZTs.

A piston accuracy experiment from 29 June 2001 is shown below. In this example, Seg. #3 was pistoned 16 times, in steps of +25 nm, for a total segment travel distance of 400 nm. At each piston position, 5 exposures were taken with the 900±20 nm filter, then dark-subtracted and co-added together. Each final co-added image was then analyzed with IPO.

Since the total segment travel distance of +400 nm is larger than the ±225 nm piston capture range, the detected piston values "wrapped" after +225 nm, thus resulting in a sawtooth graph similar to Figure 2. However, we know *a priori* that each PZT command was sent in the positively increasing direction; therefore, the detected piston values can be "manually unwrapped" by adding λ/2 to the wrapped values. The left-hand plot in Figure 5 shows the results after manual unwrapping. The uncertainty in IPO's piston sensing is given by the RSS residual of a least-squares fit to the data. In this example, the calculated residual error of ~6 nm is on the same order as the 5 nm accuracy of the PZTs. Since the global piston of the 3 segments is not observable, Seg. #1 was used as the reference segment in this analysis. Seg. #2 was allowed to drift during the experiment (square-shaped data points).

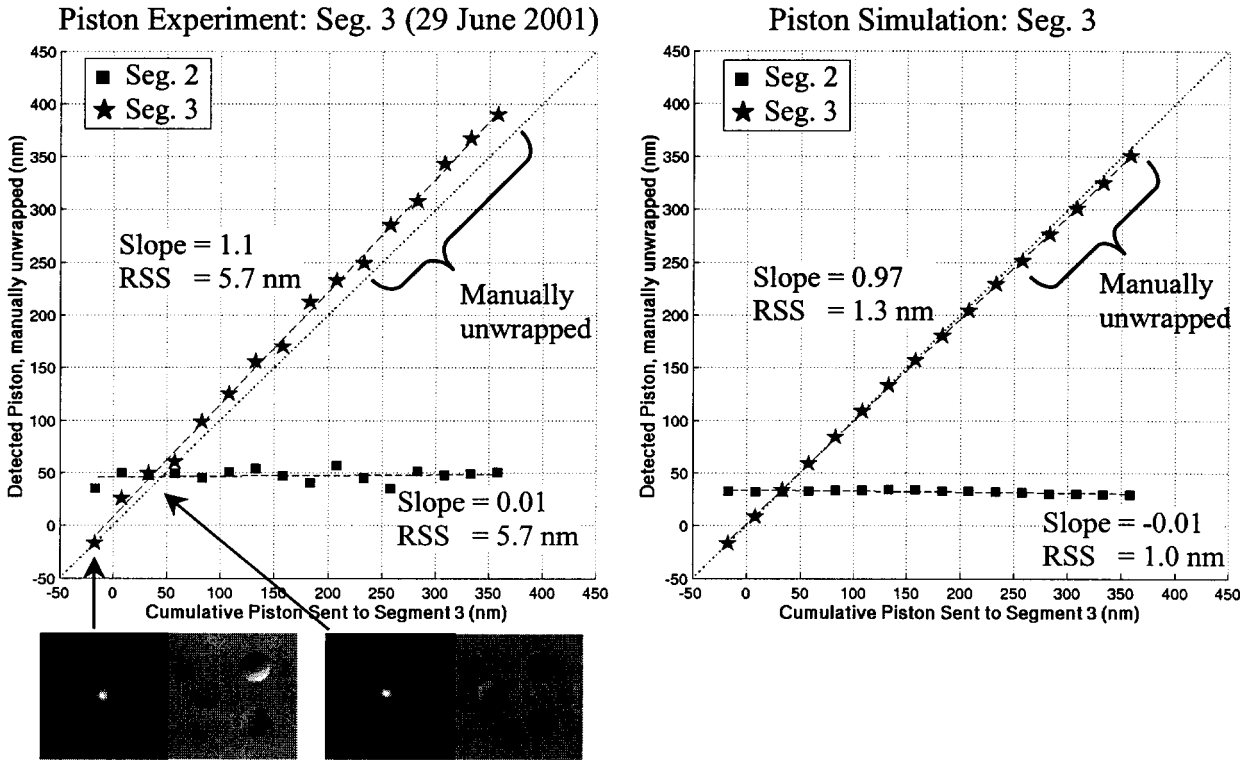

Figure 5: Piston accuracy experiment and simulation, using Seg. #3 with the PSF magnifier.

The contribution of certain noise sources to the piston sensing uncertainty (~6 nm) was studied in the simulation shown in the right-hand plot of Figure 5. In this simulation, in-focus images were generated using the WCT-2 computer model with photon noise, CCD read noise, and a Gaussian blur kernel ($\sigma_{x,y}$ = 0.54 pixels to simulate the blurring effect of the 5 micron pinhole on the testbed.) To reproduce the effect of residual aberrations, the first simulated image incorporated the measured piston, tip, and tilt values from the first data point in the experiment (left-hand plot.) In subsequent images, the Seg. #3 piston value was incremented by +25 nm. Ten PSF realizations were generated for each image. Each PSF was deliberately mis-centered to simulate the effect of residual centroiding error. The images were then processed with the same IPO software that was used in the experiment – the calculated residual error for the simulation was ~1.3 nm. Note that this simulation did not account for other potential error sources, such as lab seeing, jitter, and segment drift over time.

Tables 1 and 2 summarize our piston and tip/tilt accuracy experiments on WCT-2, both with and without the PSF magnifier. The overall piston accuracy (RSS) is about 6 nm with the magnifier, and about 9 nm without the magnifier. The overall tip/tilt accuracy with the magnifier is 0.09 arcseconds; without the magnifier, 0.28 arcseconds.

Table 1: Summary of WCT-2 accuracy experiments with the PSF magnifier.

	PISTON		X-TILT		Y-TILT	
	Slope	RSS (nm)	Slope	RSS (arcsec)	Slope	RSS (arcsec)
Seg. 1	1.09	7.5	0.93	0.07	0.89	0.07
Seg. 2	1.06	4.6	1.11	0.13	0.86	0.11
Seg. 3	1.07	5.7	1.05	0.08	0.97	0.05

Table 2: Summary of WCT-2 accuracy experiments without the PSF magnifier.

	PISTON		X-TILT		Y-TILT	
	Slope	RSS (nm)	Slope	RSS (arcsec)	Slope	RSS (arcsec)
Seg. 1	1.10	5.5	1.06	0.23	0.96	0.33
Seg. 2	1.08	9.1	1.12	0.43	1.17	0.32
Seg. 3	0.99	12.4	1.12	0.11	0.77	0.14

3.5 Two-Wavelength IPO

As described in Section 3.2, the piston capture range on WCT-2 is $\pm\lambda/4$ when the measurement is made with a single narrowband filter. By combining multiple narrowband measurements, the capture range can be significantly expanded, depending on the selected wavelengths and the associated measurement uncertainties.

The following two-wavelength IPO algorithm has been demonstrated on WCT-2. In-focus images are taken at two wavelengths, λ_1 and λ_2 (Figure 6a.) The first image is processed with the standard single-wavelength IPO algorithm to obtain a solution at λ_1 (Figure 6b.) From the computed vector of piston values, a finite set of solutions for λ_2 are obtained by considering the 8 possible combinations of adding $\lambda_1/2$ to the vector of λ_1 piston values. The top row of Figure 6c shows the λ_2 model images for the 8 candidate solutions. The bottom row shows the difference between the λ_2 data image and these model images. The best match is given by the difference image with the smallest cost function. In this example, the model image in the fourth column of Figure 6c is clearly the best match to the λ_2 data image. Finally, the λ_2 data image is processed with the single-wavelength IPO algorithm, using the piston vector obtained from step (c) as an initial starting point (Figure 6d.)

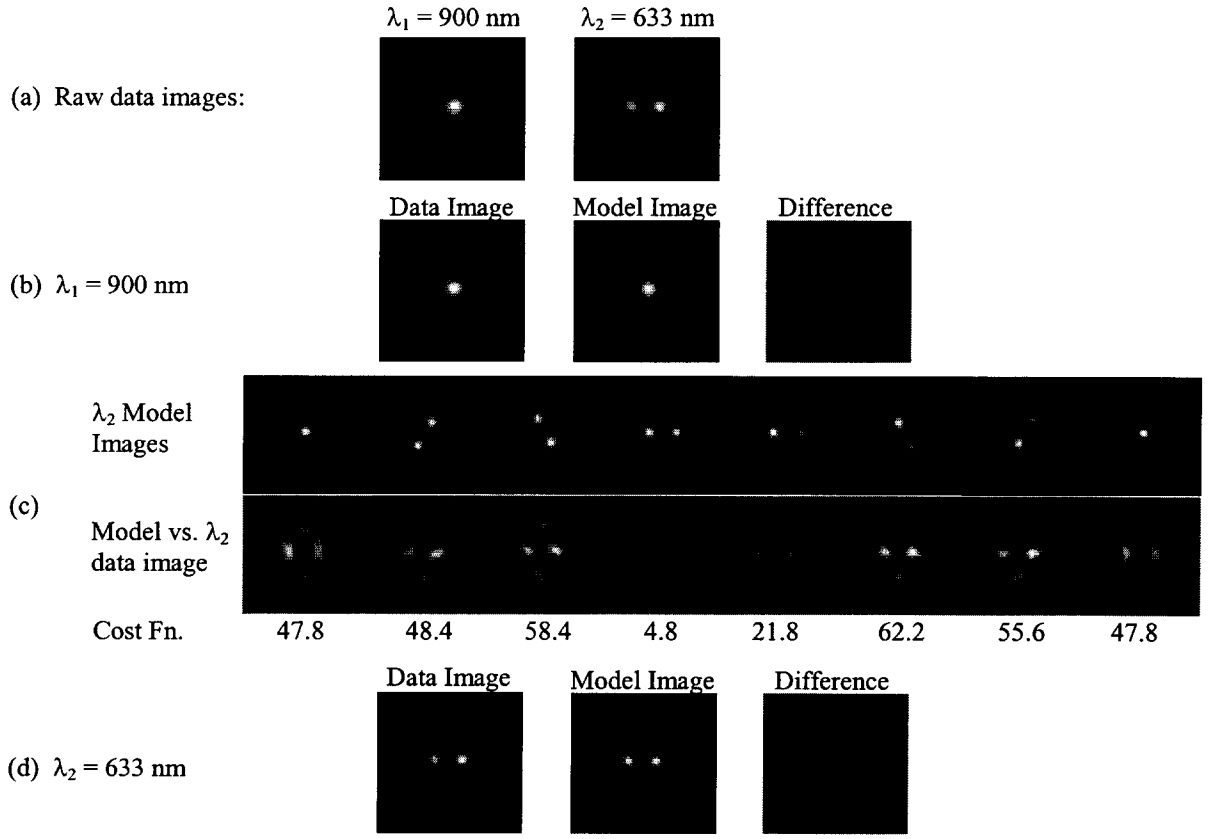

Figure 6: (a) Data images show segments phased at λ_1, but not at λ_2. (b) After analyzing λ_1 data image with standard single-wavelength IPO. (c) λ_2 model images depicting the 8 possible candidate matches for the λ_2 data image. (d) After analyzing λ_2 data image with single-wavelength IPO, using the solution in (c) as a starting guess.

The two-wavelength IPO algorithm was demonstrated on 7 September 2001. The experiment was conducted immediately after a White Light Interferometry experiment[7], so that the segments were in a well-phased position at the start of the IPO experiment. Seg. #1 was then scanned in positively increasing steps of +25 nm, over a total distance of 550 nm. At each step, in-focus images were taken at two wavelengths, 633±1.5 nm and 900±20 nm. The left-hand plot in Figure 7 shows the results of processing only the 900 nm data images with single-wavelength IPO – as expected, the detected piston values were "wrapped" after the segment height exceeded +225 nm.

The right-hand plot shows the results of processing both the 900 nm and the 633 nm data images, using the two-wavelength algorithm described above. By utilizing both images, the piston capture range was extended from ±225 nm (as provided by the 900 nm filter) to ±450 nm.

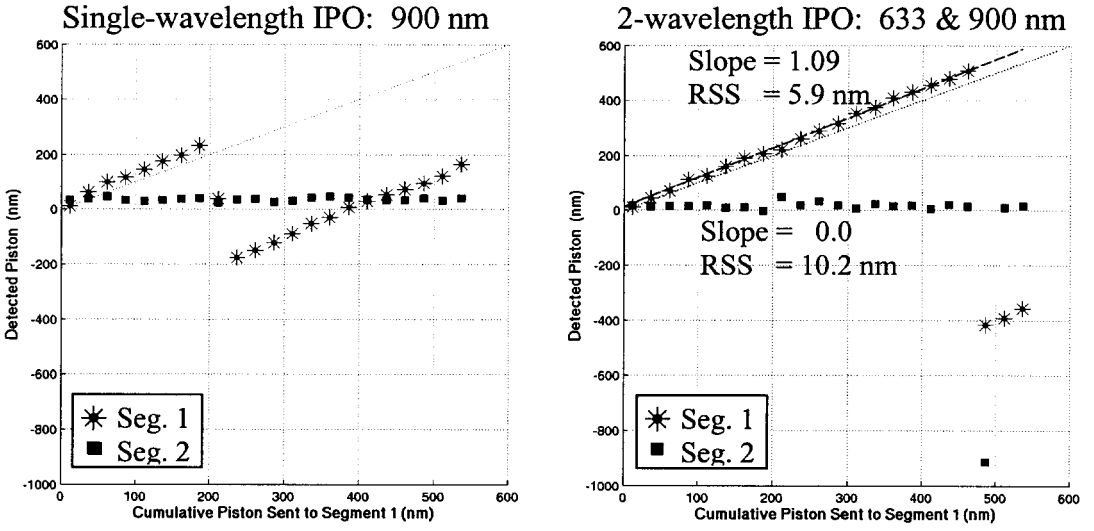

Figure 7: Two-wavelength IPO experiment.

3.6 In-Focus WFS&C Movie

A real-time PSF monitoring and control experiment was performed on 29 May 2001. This experiment demonstrated the robustness and reliability of in-focus WFS&C on WCT-2.

First, the IPO Panel in the WCT Executive Software[7] was used to phase the segments at 900 nm. Next, the mirrors were deliberately misaligned by sending random piston and tip/tilt commands to the 3 segments. An in-focus data image was acquired at 900 nm ("before" image, Figure 8a,) and processed with the IPO algorithm. The computed piston/tip/tilt corrections were then sent to the mirror segments. Finally, a post-control data image was taken to verify the segment alignment ("after" image, Figure 8b.)

Figure 8: (a) PSF and wavefront map after sending random piston/tip/tilt commands to the 3 segments. (b) After using IPO to calculate the wavefront error and send the necessary alignment commands to correct the mirror segments.

This sequence was repeated 71 times. Each iteration, including the CCD exposures, the data pre-processing and IPO analysis, and the network communication time to the WCT hardware, took about 7 minutes. For every iteration, the calculated segment corrections successfully restored the full optical quality in the PSF.

4. CLOSING REMARKS

PSF Monitoring is a technique for measuring low-order wavefront aberrations in segmented-mirror telescopes using in-focus PSF measurements. This method has been rigorously demonstrated on the segmented aperture system of the WCT hardware. The experiments presented in this paper show excellent performance in controlling the rigid-body degrees of freedom of the three mirror segments on WCT. In addition, our computer models of the system have been validated by the simulations discussed in this report, which accurately predict the capture range and detection accuracy observed on the hardware.

Continuing studies include the effects of segment aberrations, jitter, signal-to-noise, and filter bandwidth on IPO's wavefront sensing accuracy. Most of these studies will be conducted on WCT-3 and WCT-4, a planned modification of WCT that will utilize flight hardware and a filled-aperture primary mirror to be more analogous to the real NGST. Simulations have been performed for the two potential NGST designs, and the on-orbit operational aspects of PSF monitoring will be explored as well. Model validation on WCT-3 and WCT-4 will play a critical role in the continuing development of our algorithms and predicting the final performance of PSF monitoring on NGST.

ACKNOWLEDGEMENTS

This research was carried out at the Jet Propulsion Laboratory, California Institute of Technology, under a contract with the National Aeronautics and Space Administration (NASA). The authors gratefully acknowledge the support of the Wavefront Control Testbed team at the NASA Goddard Space Flight Center.

REFERENCES

1. D. C. Redding, S. A. Basinger, C. W. Bowers, R. Burg, L. A. Burns, D. Cohen, B. H. Dean, J. J. Green, A. E. Lowman, C. M. Ohara, and F. Shi, "Next Generation Space Telescope wavefront sensing and control," SPIE Paper 4850-56, Waikoloa HI (2002).
2. P. Petrone III, S. A. Basinger, C. W. Bowers, D. Cohen, L. A. Burns, A. Chu, P. S. Davila, P. Dogota, B. H. Dean, J. J. Green, K. Ha, W. L. Hayden, D. J. Lindler, A. E. Lowman, C. M. Ohara, D. C. Redding, F. Shi, M. E. Wilson, B. J. Zukowski, "Optical design and performance of the NGST wavefront control testbed," SPIE Paper 4850-55, Waikoloa HI (2002).
3. D. C. Redding, P. Dumont, J. Yu, "Hubble Space Telescope prescription retrieval," *Applied Optics-OT*, vol. 32, p. 1728 (Apr. 1993).

4. D. C. Redding, M. Levine, et al, "Modeling and Analysis for Controlled Optical Systems (MACOS) User Manual," Version 2.80 (Jet Propulsion Laboratory, California Institute of Technology, 4800 Oak Grove Drive, Pasadena, CA, 91109, 1992-1999.
5. "NanoPosition 1998," Physik Instrumente Catalog (1998).
6. F. Shi, D. C. Redding, A. E. Lowman, C. W. Bowers, L. A. Burns, P. Petrone III, C. M. Ohara, S. A. Basinger, "Segmented mirror coarse phasing with a dispersed fringe sensor: experiments on NGST's wavefront control testbed," SPIE Paper 4850-51, Waikoloa HI (2002).
7. F. Shi, D. C. Redding, A. E. Lowman, C. W. Bowers, L. A. Burns, P. Petrone III, C. M. Ohara, S. A. Basinger, "Segmented mirror coarse phasing with white light interferometry: modeling and experimenting on NGST's wavefront control testbed," SPIE Paper 4850-59, Waikoloa HI (2002).
8. S. A. Basinger, D. C. Redding, F. Shi, D. Cohen, J. J. Green, C. M. Ohara, A. E. Lowman, L. A. Burns, "Wavefront sensing and control software for a segmented space telescope," SPIE Paper 4850-56, Waikoloa HI (2002).